JACS
JOURNAL OF THE AMERICAN CHEMICAL SOCIETY
Article
pubs.acs.org/JACS

Light-Induced Changes in Magnetism in a Coordination Polymer Heterostructure, $Rb_{0.24}Co[Fe(CN)_6]_{0.74}@K_{0.10}Co[Cr(CN)_6]_{0.70}\cdot nH_2O$ and the Role of the Shell Thickness on the Properties of Both Core and Shell

Olivia N. Risset,[†] Pedro A. Quintero,[‡] Tatiana V. Brinzari,[‡] Matthew J. Andrus,[†] Michael W. Lufaso,[§] Mark W. Meisel,*[,‡] and Daniel R. Talham*[,†]

[†]Department of Chemistry, University of Florida, Gainesville, Florida 32611-7200, United States

[‡]Department of Physics and the National High Magnetic Field Laboratory, University of Florida, Gainesville, Florida 32611-8440, United States

[§]Department of Chemistry, University of North Florida, Jacksonville, Florida 32224-7699, United States

Supporting Information

ABSTRACT: Particles of formula $Rb_{0.24}Co[Fe(CN)_6]_{0.74}@K_{0.10}Co[Cr(CN)_6]_{0.70}\cdot nH_2O$ with a light-responsive rubidium cobalt hexacyanoferrate (RbCoFe) core and a magnetic potassium cobalt hexacyanochromate (KCoCr) shell have been prepared and exhibit light-induced changes in the magnetization of the normally light-insensitive KCoCr shell, a new property resulting from the synergy between the core and shell of a coordination polymer heterostructure. A single batch of 135 ± 12 nm RbCoFe particles are used as seeds to generate three different core@shell samples, with KCoCr shell thicknesses of approximately 11, 23 and 37 nm, to probe the influence of the shell thickness over the particles' morphology and structural and magnetic properties. Synchrotron powder X-ray diffraction reveals that structural changes in the shell accompany the charge transfer induced spin transition (CTIST) of the core, giving direct evidence that the photomagnetic response of the shell is magnetomechanical in origin. The depth to which the KCoCr shell contributes to changes in magnetization is estimated to be approximately 24 nm when using a model that assumes a constant magnetic response of the core within the series of particles. In turn, the presence of the shell changes the nature of the CTIST of the core. As opposed to the usually observed first order transition exhibiting hysteresis, the CTIST becomes continuous in the core@shell particles.

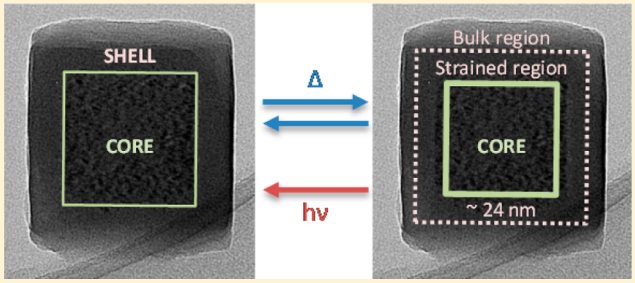

INTRODUCTION

Whether described as network solids or as metal organic frameworks, studies of coordination polymer solids extend to catalysis, ion transport and storage, gas separations and storage, electrochromism, negative thermal expansion, magnetism and light switchable magnetism.[1−13] Work on these solid-state topics parallels efforts looking at biomedical applications of coordination polymers such as nanocarriers for drug delivery, contrast agents for MRI or for X-ray computed tomography, optical biomarkers or therapeutic agents.[11,14−18] Many of these applications benefit from producing nanoscale or mesoscale structures or from understanding interactions at these length scales.

The study of nanoscale or mesoscale heterostructures of coordination polymers is in its infancy, but just as for more traditional solid-state materials, coordination polymer heterostructures provide routes to do more than simply combine properties. Synergy between components can lead to new behaviors, and an example is in the area of lithium ion storage using cyanometallate "Prussian blue analogues" (PBAs). The analogue $K_{0.1}Cu[Fe(CN)_6]_{0.7}\cdot 3.8H_2O$ has high storage capacity, but the capacity degrades with successive redox cycling.[19,20] However, adding a shell of a second analogue leads to enhanced performance as the presence of the shell suppresses a cubic to tetragonal phase change associated with the Cu^+/Cu^{2+} redox couple of the pure phase.[21,22] New behavior is also seen in magnetic heterostructures of Prussian blue analogues. The nickel hexacyanochromates are not light responsive, but when incorporated into heterostructure thin films or core@shell particles with light switchable spin-transition compounds such as the Prussian blue analogue cobalt hexacyanoferrate or the Hofmann-like phase $Fe(azpy)[Pt(CN)_4]\cdot nH_2O$, their magnetization can be altered with light as a result of magneto-mechanical[23] coupling across the interface between the components.[24−29]

Received: August 17, 2014
Published: October 6, 2014

   dx.doi.org/10.1021/ja5084283 | J. Am. Chem. Soc. 2014, 136, 15660−15669

With these examples of new behavior arising from forming an interface between two coordination polymer components, it becomes important to perform systematic explorations into the influence of the interface in these classes of materials. In this paper, we report the synthesis and characterization of a new type of PBA core@shell heterostructure, $Rb_{0.24}Co[Fe(CN)_6]_{0.74}@K_{0.10}Co[Cr(CN)_6]_{0.70}\cdot nH_2O$ (RbCoFe@KCoCr). The system was chosen to extend light switchable magnetism to new examples as the RbCoFe analogue is light responsive and the KCoCr analogue is a ferromagnet with $T_c \sim 30$ K.[30] The family of cobalt hexacyanoferrates undergoes a well characterized charge-transfer induced spin transition (CTIST) that can be either thermally or optically activated.[31−41] The transition, Fe^{2+}-CN-$Co^{3+}_{(LS)} \rightarrow Fe^{3+}$-CN-$Co^{2+}_{(HS)}$, involves a spin change on the Co^{2+} ion, significantly lengthening the Co−N bond and leading to an expansion of the lattice. When the charge transfer reverses, the lattice contracts. This elastic process in the core is thought to induce a magnetomechanical response in the magnetic shell.[23]

In support of this mechanism, direct evidence for a structural change in the shell in response to the CTIST of the core is provided by temperature-dependent X-ray diffraction. In addition, the new core@shell system leads to insights into the influence of the interface on the morphology and properties of the heterostructure, and in particular how these features change as the shell becomes thicker. The epitaxial relationship between core and shell in heterostructures containing two different Prussian blue analogues was previously reported.[42,43] Here, a method was developed to prepare a series of core@shell particles with different shell thicknesses, starting from a common batch of narrowly disperse core particles. For RbCoFe@KCoCr, the preference for growth on the (100) faces is demonstrated. With this series of particles in hand, it is possible to estimate the depth to which the magnetic properties of the shell are altered by the presence of an interface with the core particles that undergo a light-induced structural change. Furthermore, an influence of the shell on the behavior of the core is also observed. The KCoCr shell changes the nature of the structural transition associated with the RbCoFe thermal CTIST. Normally a discontinuous, first-order transition in the single phase RbCoFe, the presence of the shell leads to a continuous phase transition in the core@shell particles.

EXPERIMENTAL SECTION

Material Preparation. All chemical reagents were purchased from Sigma-Aldrich and used without further purification. Deionized water was used as solvent in all the following procedures.

RbCoFe Core Particles. In a typical experiment, 200 mL of an aqueous solution containing $CoCl_2.6H_2O$ (95 mg; 0.40 mmol) and RbCl (95 mg; 0.79 mmol) were added dropwise (3.5 mL/min) to an equal volume of an aqueous solution containing $K_3[Fe(CN)_6]$ (150 mg; 0.46 mmol). After maturation for 4 h under vigorous stirring, the particles were centrifuged at 9000 rpm for 10 min and subsequently washed with 300 mL of water. The particles were redispersed in 400 mL of water to give the suspension of core particles. Except for a 5 mL aliquot used for characterization, the particles were not isolated and the suspension was used immediately in the next step.

$Rb_{0.24}Co[Fe(CN)_6]_{0.74}\cdot 3H_2O$ (RbCoFe). Dark purple suspension (97% yield based on isolated batches). IR (KBr): 2162 (νCN, Co^{II}-NC-Fe^{III} high spin (HS)), 2110 (sh, νCN, Co^{III}-NC-Fe^{II} low spin (LS)), 2098 (νCN, Co^{II}-NC-Fe^{II}) cm^{-1}. EDS: 0.24:1.0:0.74 (Rb:Co:Fe). Anal. Calcd for: C, 18.37; H, 2.07; N, 21.43. Found: C, 18.06; H, 1.92; N, 20.96.

RbCoFe@KCoCr Core@Shell Particles; a_s (Average Shell Thickness) = 11 nm (1). $CoCl_2\cdot 6H_2O$ (48 mg; 0.20 mmol) dissolved in 50 mL of water and an equal volume of an aqueous solution containing $K_3[Cr(CN)_6]$ (75 mg; 0.23 mmol) were simultaneously added (8 mL/h using a peristaltic pump) to the core particle suspension under vigorous stirring for 15 h. The particles were isolated by centrifugation at 9000 rpm for 10 min and subsequently washed with 300 mL of water. The product was divided in two equal portions; one-half was isolated and air-dried while the other half was redispersed in 350 mL of water to be used as seeds in the following experiment.

$\{Rb_{0.24}Co[Fe(CN)_6]_{0.74}\}_{0.67}@\{K_{0.10}Co[Cr(CN)_6]_{0.70}\}_{0.33}\cdot 3.5H_2O$. Dark purple powder (86 mg; 98% yield). IR (KBr): 2162 (asymmetric broadening, νCN, Co^{II}−NC-Cr^{III}, Co^{II}-NC-Fe^{III}), 2110 (sh, νCN, Co^{III}-NC-Fe^{II}), 2097 (νCN, Co^{II}-NC-Fe^{II}) cm^{-1}. EDS: 0.03:0.16:1.00:0.50:0.23 (K:Rb:Co:Fe:Cr); KCoCr:RbCoFe = 0.49. Anal. Calcd for: C, 18.04; H, 2.40; N, 21.04. Found: C, 17.62; H, 2.26; N, 20.67.

RbCoFe@KCoCr Core@Shell Particles; a_s = 23 nm (2). $CoCl_2\cdot 6H_2O$ (33 mg; 0.14 mmol) dissolved in 35 mL of water and an equal volume of an aqueous solution containing $K_3[Cr(CN)_6]$ (53 mg; 0.16 mmol) were simultaneously added (8 mL/h using a peristaltic pump) to the particle suspension (**1**) under vigorous stirring for 15 h. The particles were isolated by centrifugation at 9000 rpm for 10 min and subsequently washed with 300 mL of water. The product was divided in two equal portions; one-half was isolated and air-dried while the other half was redispersed in 250 mL of water to be used as seeds in the following experiment.

$\{Rb_{0.24}Co[Fe(CN)_6]_{0.74}\}_{0.46}@\{K_{0.10}Co[Cr(CN)_6]_{0.70}\}_{0.54}\cdot 3.7H_2O$. Purple powder (56 mg; 89% yield). IR (KBr): 2163 (asymmetric broadening, νCN, Co^{II}−NC-Cr^{III}, Co^{II}-NC-Fe^{III}), 2110 (sh, νCN, Co^{III}-NC-Fe^{II}), 2097 (νCN, Co^{II}-NC-Fe^{II}) cm^{-1}. EDS: 0.05:0.12:1.00:0.34:0.37 (K:Rb:Co:Fe:Cr); KCoCr:RbCoFe = 1.15. Anal. Calcd for: C, 17.96; H, 2.57; N, 20.95. Found: C, 17.59; H, 2.44; N, 20.54.

RbCoFe@KCoCr Core@Shell Particles; a_s = 37 nm (3). $CoCl_2\cdot 6H_2O$ (33 mg; 0.14 mmol) dissolved in 35 mL of water and an equal volume of an aqueous solution containing $K_3[Cr(CN)_6]$ (53 mg; 0.16 mmol) were simultaneously added (8 mL/h using a peristaltic pump) to the particle suspension (**2**) under vigorous stirring for 15 h. The particles were isolated by centrifugation at 9000 rpm for 10 min and subsequently washed with 300 mL of water. The product was isolated and air-dried.

$\{Rb_{0.24}Co[Fe(CN)_6]_{0.74}\}_{0.28}@\{K_{0.10}Co[Cr(CN)_6]_{0.70}\}_{0.72}\cdot 4H_2O$. Light purple powder (83 mg; 81% yield). IR (KBr): 2165 (asymmetric broadening, νCN, Co^{II}−NC-Cr^{III}, Co^{II}-NC-Fe^{III}), 2110 (sh, νCN, Co^{III}-NC-Fe^{II}), 2097 (νCN, Co^{II}-NC-Fe^{II}) cm^{-1}. EDS: 0.07:0.06:1.00:0.20:0.49 (K:Rb:Co:Fe:Cr); KCoCr:RbCoFe = 2.59. Anal. Calcd for: C, 17.76; H, 2.77; N, 20.72. Found: C, 17.31; H, 2.57; N, 20.37.

Characterization. Fourier transform infrared spectroscopy (FT-IR) was performed on a Nicolet 6700 Thermo Scientific spectrophotometer taking 16 scans per spectrum between 4000 and 400 cm^{-1} with a resolution of 0.482 cm^{-1}. Samples were placed onto the face of a KBr pellet by dispersing 1 mg of powder in acetone and dropping the dispersion onto the preformed pellet. The spectrum of a pure KBr pellet is taken as a background reference. Transmission electron microscopy (TEM) was performed on a JEOL-2010F high-resolution transmission electron microscope at 200 kV. The TEM samples were prepared by dropping 40 μL of a water solution (1 mL) containing 2 mg of product, dispersed by sonication, onto the grid (carbon film on a holey carbon support film, 400 mesh, copper from Ted-Pella, Inc.). Energy-dispersive X-ray spectroscopy (EDS) was performed with an Oxford Instruments EDS X-ray Microanalysis System coupled to the high-resolution TEM (HRTEM) microscope. A total of four scans were recorded on different parts of the sample and then averaged to give relative atomic percentages for the metallic elements. Combustion analysis to determine carbon, hydrogen, and nitrogen (CHN) contents was performed at the University of Florida Spectroscopic Services Laboratory on an EA1108 CHNS-O manufactured by Fisons Instruments in 1995. Chemical formulas are

dx.doi.org/10.1021/ja5084283 | J. Am. Chem. Soc. 2014, 136, 15660−15669

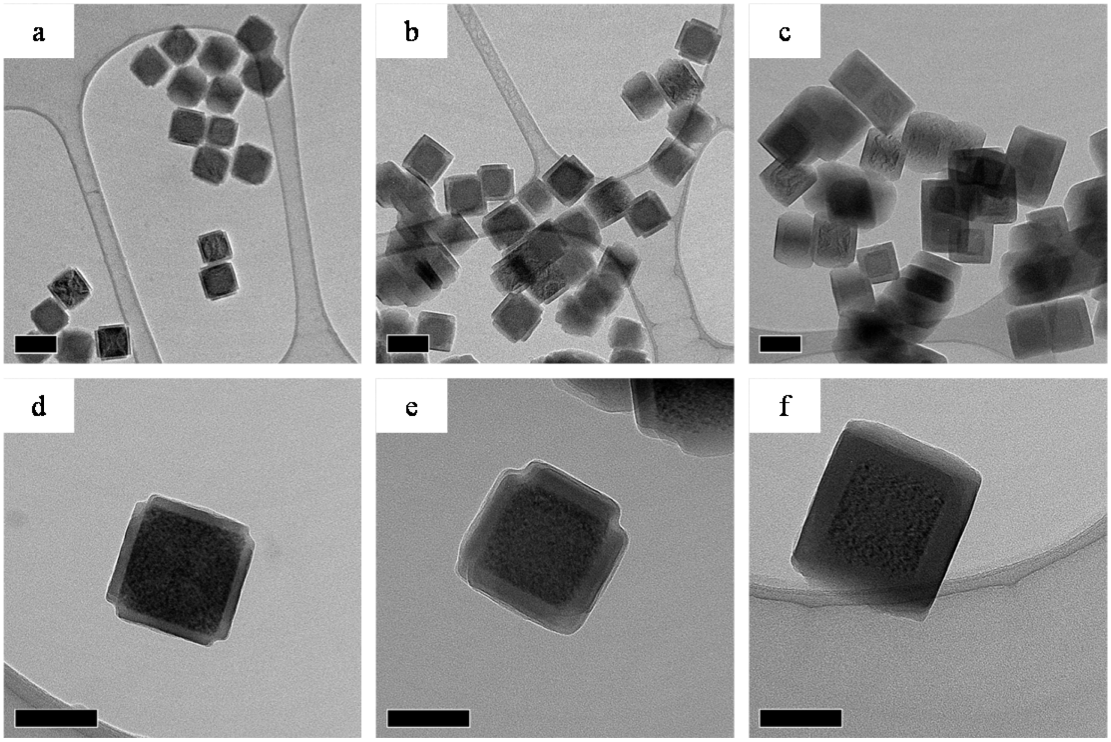

Figure 1. TEM images of RbCoFe@KCoCr core@shell nanoparticles. The average shell thickness (t) is defined as half the difference between the edge-to-edge distance of the core@shell particles and the corresponding distance for the cores. With t = 11 nm, **1** shows an unprecedented cross shape (a, d). By increasing t to 23 nm, the morphology of **2** evolves toward the expected cubic shape (b, e). Further increasing t to 37 nm, **3** displays exclusively the cubic morphology (c, f). Scale bars for frames a–c are 200 nm, and for d–f the scale bars are 100 nm.

based on the metal compositions from EDS as well as the elemental analysis. The particle size distribution is determined from the size measurements of a minimum of 200 particles from multiple regions in one sample. The particle size is reported as the mean along with the standard deviation as determined by descriptive statistics performed in Origin 8.5. The average shell thickness is defined as half of the difference between the size of the core@shell particles and the size of the cores. Powder X-ray diffraction (PXRD) was performed at Argonne National Laboratory on the beamline 17. Each sample was loaded in a Kapton capillary and mounted on the beamline. The experimental configuration of 17-BM uses a flat panel amorphous-Si area detector positioned 500 mm from the sample. X-ray (λ = 0.72808 Å) exposure times were no less than five seconds. During each exposure the sample was rocked a total of 5 degrees. Data collection was continuous with temperature ramping between 100 and 300 K (2 K/min) with a cryostream nitrogen blower regulating the temperature. The data were processed using the FullProf Suite and fit2d which was used for the design of the stacked plots. The patterns were fitted using Le Bail method through GSAS. The magnetic properties were investigated using a commercial superconducting quantum interference device (SQUID) magnetometer (Quantum Design MPMS-XL7). The low temperature measurements were performed with the powder samples spread between two pieces of transparent tape and mounted in a homemade quartz optic sample rod[44] connected to a tungsten halogen lamp (400–2200 nm), while the high temperature measurements were performed with the sample in a gel cap inside a drinking straw in a commercial sample rod. The field-cooled temperature dependence of the magnetization was measured in an applied field of 100 G while warming, in the 5–40 K region. After isothermal irradiation at 5 K and 100 G, irradiation was ceased and the light state established. The magnetization of the light state was measured in the temperature range 5–40 K while warming. The high temperature measurements were performed for the dark state while warming and cooling in 100 G field in the 150–300 K region. The sweeping rate of the temperature for all the measurements was 2 K/min in the 100–300 K region and 5 K/min below 100 K.

RESULTS

Synthesis and Morphology. RbCoFe nanoparticles are synthesized as a self-stabilized suspension in water, adapting the method developed by Catala and co-workers[45] to yield uniform particles with a controllable composition in the mesoscale, typically 50–500 nm, size regime. The particles are not passivated with any stabilizer, so their surface remains chemically active and can be used to form multicomponent heterostructures. Core@shell heterostructures are prepared[25,27,42,46] by the slow addition of low concentration precursor solutions to the suspension of the uncoated particles, leading to the heterogeneous precipitation of the shell material while preventing side nucleation. Once the initial batch of core@shell particles were prepared, part of the batch was harvested for measurements and characterization while the rest was used for augmenting the KCoCr shell. The process was then cycled a third time to result in a series of three RbCoFe@KCoCr samples with increasing shell thickness, all derived from the same batch of RbCoFe core particles.

The particle morphology is nicely visualized with TEM (Figure 1), while the chemical assignments and layer segregation within the heterostructures are confirmed by EDS line scans (Supporting Information, Figure S1). The uncoated RbCoFe particles are well-defined cubes, uniform in size, 135 ± 12 nm (Supporting Information, Figure S2). Upon growth of the thinnest shell, core@shell sample **1**, the particle size increases to 157 ± 11 nm. Strikingly, **1** exhibits an intricate cross morphology as opposed to the normally observed cubic shape, indicating that the shell initially grows on the (100) faces.[43] Parenthetically, the initial absence of layer growth in the corners of the cross is a natural consequence of the "corner"-regions possessing increased strain due to the confluence of two

dx.doi.org/10.1021/ja5084283 | J. Am. Chem. Soc. 2014, 136, 15660–15669

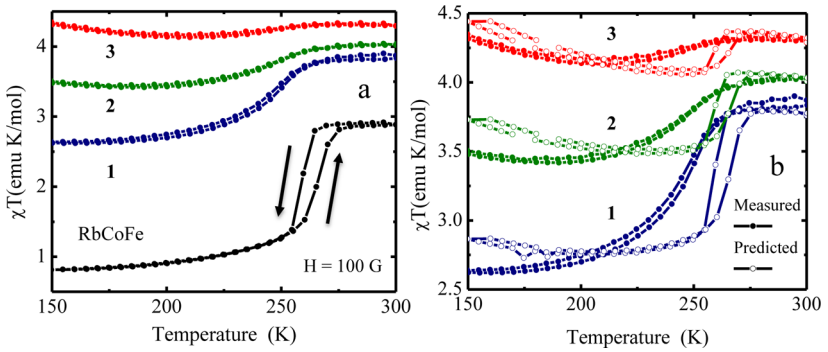

Figure 2. (a) χT vs T plots for the cooling and warming cycles under a field of 100 G in the region of the thermal CTIST for uncoated RbCoFe, and RbCoFe@KCoCr samples **1**, **2** and **3**, with an average shell thickness of, respectively, 11, 23 and 37 nm. Data were collected while cooling and warming at 2 K/min in an applied field of 100 G. All the samples display a decrease in the χT value upon cooling, consistent with the occurrence of the CTIST in the RbCoFe cores. (b) Measured (filled dots) and predicted (empty dots) low field magnetic responses in the range 150−300 K. The simulation is based on the superposition of the core and shell responses assuming both materials behave independently (see Supporting Information, Figure S10). At 300 K, the predicted values differ in less than 0.04 emu K/mol from the measured values, suggesting that, at this temperature, (i) the core and shell behave as two independent magnetic components; (ii) the core is in the HS state. At 150 K, the measured χT values are slightly lower than the values predicted by the simulation, which indicates that the core undergoes a complete transition to the LS state in all three core@shell structures.

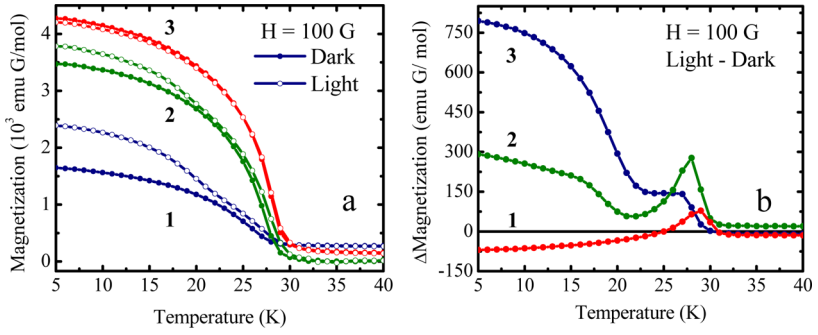

Figure 3. (a) Field-cooled magnetization vs temperature for RbCoFe@KCoCr **1**, **2** and **3** under an applied field of 100 G in the dark state (filled dots) and in the light state after irradiation at 5 K (empty dots). (b) ΔMagnetization (light−dark) vs temperature for RbCoFe@KCoCr **1**, **2** and **3**. The feature between 25 and 31 K is attributed to a modification of the superexchange in the distorted interfacial KCoCr upon irradiation, hence affecting the ordering temperature. Below 24 K, ferrimagnetic ordering of the RbCoFe cores results in further increase of ΔMagnetization in **1** and **2**, whereas a decrease is observed in **3**. For all samples, light-induced changes are observed up to 30 K, the ordering temperature of the normally nonphotomagnetic layer.

orthogonal faces.[43,47] Upon increasing the shell thickness to give a particle size of 181 ± 12 nm, core@shell sample **2**, the morphology evolves from cross-like to cubic. Further increasing the shell thickness, core@shell sample **3** exhibits the common cubic shape with a particle size of 208 ± 13 nm. For all three samples, the mean size agrees well with expectations assuming quantitative heterogeneous precipitation (Supporting Information, Figure S3, Table S4).

Signatures of two different Prussian blue analogues are seen in infrared spectroscopy, which also conveys the valence states of the metal ions in the RbCoFe core (Supporting Information, Figure S5). The FT-IR spectrum of the uncoated RbCoFe sample features characteristic bands at 2162, 2110, and 2098 cm^{-1} in the cyanide stretching region, attributed to Co^{II}-NC-Fe^{III} (high spin), Co^{III}-NC-Fe^{II} (low spin) and Co^{II}-NC-Fe^{II} sites, respectively.[31,34,37] The presence of mixed valences is consistent with the cobalt:iron ratio of the cores (Co:Fe = 1.35).[37] As the thickness of the KCoCr shell increases, the peak at 2162 cm^{-1} shifts to 2165 cm^{-1} and becomes more intense with asymmetric broadening that results from the overlap between the RbCoFe band and a KCoCr band centered at 2168 cm^{-1}.[30,48]

Powder X-ray diffraction (PXRD) patterns collected at 300 K can be indexed to two different Prussian blue-like face centered cubic lattices in the space group $Fm\bar{3}m$ (No. 225) (Supporting Information, Figure S6, Table S8). The absence of peaks corresponding to a mixed phase in the core@shell particles further confirms the segregation of the core and shell materials. The smallest lattice constant, observed at a = 10.298−10.305 Å, is characteristic of predominantly high spin RbCoFe, in good agreement with the elemental composition and the FT-IR cyanide stretches.[31,34,37,38,40] The largest lattice constant, a = 10.531−10.551 Å, is attributed to KCoCr.[42,48,49] For both core and shell components, the lattice constants are in good agreement with the single phase materials. This observation suggests that, at 300 K, despite the lattice misfit between core and shell, a structural relaxation occurs at the interface preventing uniform strain.

Magnetization Measurements. The temperature-dependent magnetic susceptibility over the temperature range 150−300 K provides information about the RbCoFe spin state and the influence of the shell thickness on the CTIST. Plots of χT vs T for the uncoated RbCoFe sample and for the RbCoFe@KCoCr heterostructures (Figure 2) each show a decrease in the χT product upon cooling, indicative of the

dx.doi.org/10.1021/ja5084283 | J. Am. Chem. Soc. 2014, 136, 15660−15669

conversion of the RbCoFe core from the paramagnetic high spin (HS) state to the diamagnetic low spin (LS) state as a result of the CTIST. The transition temperature is in the range 240−260 K for each sample. As the shell grows thicker, there is an increase in the high temperature χT values due to the larger contribution of the ferromagnetic KCoCr shell, which in this temperature range also masks the decrease in χT due to the CTIST of the RbCoFe core (Figure 2a). However, simulating the change in χT based on the superposition of the core and shell magnetic responses in Figure 2b reveals that the magnitude of the decrease is the same for each sample, confirming that the transition is complete for both the uncoated particles and the core@shell particles. Details of this analysis are in the Supporting Information.

The low-temperature behavior is shown in Figure 3, plotted as temperature-dependent field-cooled magnetization, taken both in the dark state and after white light irradiation. The isothermal magnetization curves collected at 5 K in the dark and light states are presented in the Supporting Information (Figure S11). Each of the RbCoFe@KCoCr heterostructure samples, **1**−**3**, undergoes the characteristic ferromagnetic ordering of KCoCr with the magnetization increasing below $T_c \sim 30$ K in proportion to the shell thickness. In the light state, the thinner shell samples **1** and **2** show another inflection below 25 K, attributed to ordering of the photogenerated Co^{II}−Fe^{III} moments in the RbCoFe cores. On the other hand, the sample with the thickest shell does not undergo a light-induced enhancement below 25 K, but rather shows a small light-induced decrease in magnetization. Although smaller in magnitude, this decrease is reminiscent of the photoinduced decrease previously observed for core@shell particles and thin film heterostructures combining cobalt hexacyanoferrates with nickel hexacyanochromates (KNiCr).[24−26,28,29]

These changes with light are seen more clearly in plots of ΔM, $M^{light} - M^{dark}$, in Figure 3b. Each of the core@shell systems undergoes a light-induced increase in magnetization at temperatures corresponding to the magnetic ordering of the KCoCr shell. For the thin shells, this increase persists down to the ordering temperature of the RbCoFe core. The light-induced increase at the KCoCr ordering temperature, discussed below, can be attributed to alterations of local exchange constants in the shell that occur when the core undergoes the optically induced CTIST.[28] The photoincrease near 30 K is also observed for the thickest shell sample, before crossing over to a negative ΔM at lower temperatures, as mentioned above.

Temperature-Dependent Powder X-ray Diffraction. Structural changes associated with the thermal CTIST were investigated with PXRD data obtained with a synchrotron source at the APS beamline 17-BM. The uncoated RbCoFe and the three core@shell samples are compared in Figure 4 at 300 and 160 K, above and below the transition, highlighting the (200) reflections of the cubic lattices. At 300 K, the lattice constant for the RbCoFe core in the core@shell heterostructures is consistent with the value measured for the uncoated particles (Supporting Information, Table S8). Upon cooling, a significant contraction of the RbCoFe lattice occurs as a result of the CTIST. However, at 160 K, the decrease in lattice parameter associated with the conversion from the HS to the LS state becomes smaller as the shell grows thicker. The difference in cell parameters between 300 and 160 K for the uncoated RbCoFe is $\Delta a = 0.359$ Å, whereas this value decreases to $\Delta a = 0.226$ Å for **3** (Supporting Information, Figure S7, Table S8). As the KCoCr shell becomes thicker, the lattice change associated with the RbCoFe CTIST becomes limited.

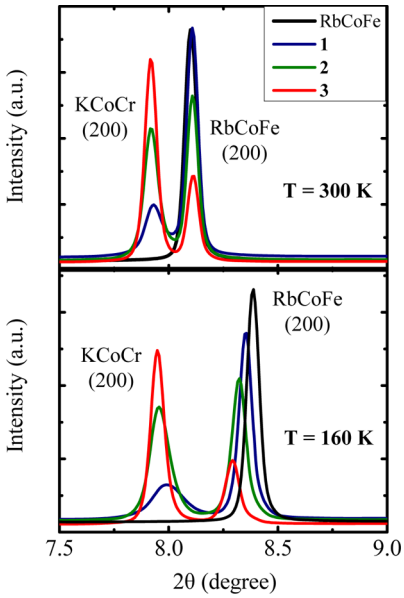

Figure 4. PXRD patterns at 300 K (top) and 160 K (bottom) for uncoated RbCoFe and RbCoFe@KCoCr samples **1**, **2** and **3**. For clarity purposes, only the (200) reflections are shown. At 300 K, the lattice constant for the RbCoFe is mainly unaffected by the presence of the shell. At 160 K, the change in lattice parameter associated with the conversion from the HS to the LS state becomes smaller as the shell thickness increases, providing evidence of a structural constraint resulting from the growth of the shell.

Additional insight is garnered by monitoring the PXRD patterns during the transition and Figure 5 presents stack plots of the temperature evolution of the (200) reflection for the uncoated RbCoFe and core@shell sample **2** while cooling from 300 to 160 K. The stack plots for core@shell samples **1** and **3** are presented in the Supporting Information (Figure S9). Centered near 250 K, the uncoated RbCoFe shows the expected discontinuous transition, meaning reflections for the HS state diminish as the reflections for the LS state intensify. At 160 K, only the signals arising from the LS state are observed suggesting a complete conversion. In contrast, the temperature dependence of the diffraction pattern for the RbCoFe within the core@shell architecture evolves differently. The core of the RbCoFe@KCoCr heterostructures undergoes the CTIST mainly through a continuous phase transition. Figure 5b follows the (200) reflections of both the RbCoFe core and the KCoCr shell upon cooling. The PXRD pattern displays a gradual shift of the Bragg reflections attributed to the RbCoFe cores. Instead of the HS state diminishing as the LS state appears, at any one temperature through the transition, only one intermediate lattice spacing is detected. Clearly, the nature of the transition has changed in the core@shell heterostructure. The (200) reflection of the shell also displays a shift, although to a much smaller extent than the CTIST active RbCoFe core. Nevertheless, a shift in position along with a slight broadening of the KCoCr Bragg peaks provides evidence of an elastic influence on the shell when the RbCoFe core undergoes the CTIST (Supporting Information, Table S8).

The change in lattice constant associated with the thermal CTIST is reversed upon light irradiation at low temperatures. Figure 6 compares the 200 reflections of the core and shell of sample **1** at 300, 160, and 100 K after irradiating with white

dx.doi.org/10.1021/ja5084283 | J. Am. Chem. Soc. 2014, 136, 15660−15669

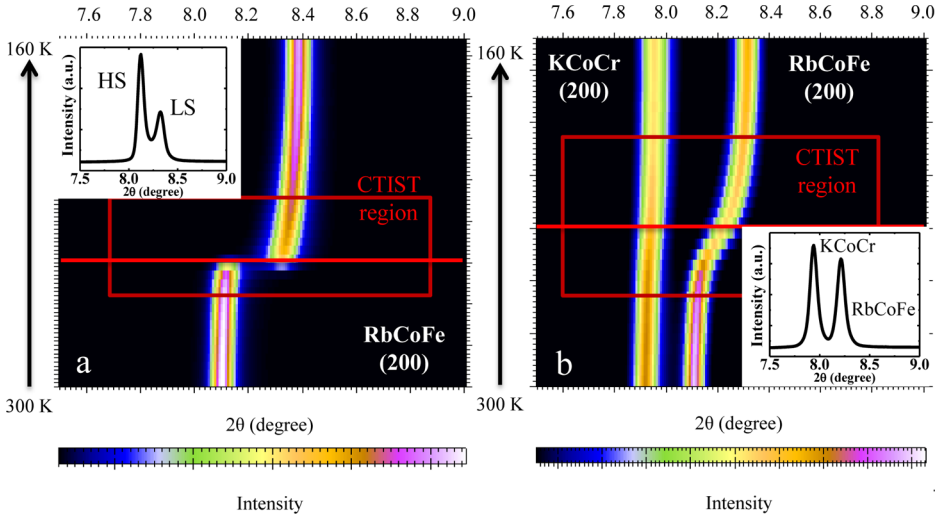

Figure 5. (a) PXRD patterns collected every 4 K and stacked as a function of temperature, from 300 to 160 K, for the uncoated RbCoFe. The RbCoFe particles undergo the CTIST through a discontinuous, first order phase transition. The inset corresponds to the PXRD pattern marked by a red line in the stacked plot and shows the coexistence of individual signals corresponding to both HS and LS states, characteristic of a first-order transition. (b) PXRD patterns collected every 5 K and stacked as a function of temperature, from 300 to 160 K, for the RbCoFe@KCoCr sample, **2**. The reflection at a lower angle corresponds to KCoCr and the signal at higher angle is characteristic of RbCoFe. The RbCoFe core within the core@shell architecture undergoes the CTIST through a continuous phase transition. The inset corresponds to the PXRD pattern marked by a red line in the stacked plot and shows only one reflection attributed to the RbCoFe core that gradually shifts upon cooling. For clarity, only a small region of the PXRD patterns is shown, focusing on the (200) reflection.

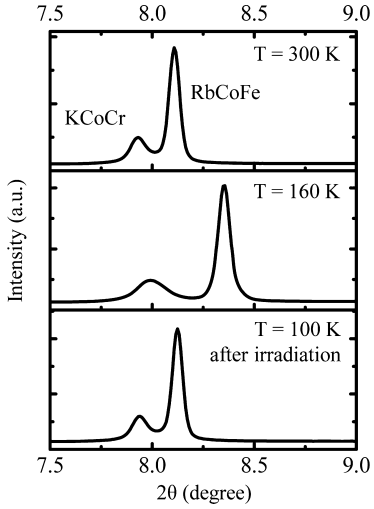

Figure 6. PXRD patterns for **1**, showing the (200) reflection, collected at 300, 160 and 100 K after irradiation with white light. Upon cooling, the contraction of the RbCoFe unit cell associated with the thermal CTIST induces structural strains on the KCoCr shell as illustrated by the broadening and shift to higher angle of the shell reflections. The changes in both the core and shell material are reversed after irradiation with light at 100 K.

light. The core is converted back to the high spin phase, and at the same time, the changes in the shell are reversed. In Figure 6, the 200 peak of the KCoCr shell, which is shifted and broadened at 160 K, returns to its original position and shape after irradiation.

DISCUSSION

Controlling Magnetism of the Shell Material. The design of heterostructures that combine the photoactive CoFe PBA with a compound that orders magnetically at higher temperature has proven a successful strategy for developing magnetic materials that can be switched with light.[24−27] The previous examples involved KNiCr as the normally non-photoactive magnetic component in either core@shell or thin film heteostructures. A goal of the present work is to extend the concept to other heterostructures by coupling the CoFe PBA with a different magnetic component, in this case KCoCr, which orders ferromagnetically at approximately 30 K.[30] Indeed, changes are observed in the magnetization of the KCoCr shell in response to the light-induced CTIST of the RbCoFe core.

The previously studied RbCoFe/KNiCr heterostructures all showed a light-induced decrease of magnetization of the KNiCr component.[24−26,28] Although to a lesser extent, a similar result is observed for the core@shell sample **3**, as shown in Figure 3. For the thickest shell sample, there is a light-induced decrease in magnetization at lowest temperatures as a result of the demagnetization of the KCoCr shell at the interface. A question arises about why the thinner shelled heterostructures do not show this light-induced decrease, only showing the photo-induced increase attributed to the RbCoFe core. As will be explained below, in these cases, changes in the thinner shells are masked by the larger volume core.

The light-induced decrease can be attributed to magneto-mechanical effects resulting from the interface between the two components.[23] Light-induced, as well as thermally induced, changes in the structure of the core are transmitted to the shell across the interface, altering magnetism.[43,47] Evidence for the shell undergoing structural changes can be seen in Figure 5, where the (200) reflection of the shell broadens and moves to higher 2θ as the core undergoes the thermal CTIST, from high spin to low spin, at around 250 K. At 160 K, the shift of the shell reflections to higher 2θ accompanies a significant decrease of the KCoCr unit cell, which evidence the presence of uniform strain throughout the shell (see Supporting Information, Table S8). As the shell grows thicker, the decrease in lattice constant upon cooling is closer to the value expected for thermal

dx.doi.org/10.1021/ja5084283 | J. Am. Chem. Soc. 2014, 136, 15660−15669

contraction only. This observation is consistent with the more bulk-like behavior of the thickest shell, as is further described in more detail using a 3-component model.

Additional information pertaining to the mechanism of line broadening can be obtained from a Williamson−Hall analysis applied to the line width of each set of reflections associated with the core and shell.[50] This method deconvolutes the size-induced broadening related to the crystallite size (L_c) and the broadening due to nonuniform strain (ε) as a function of the Bragg angle, θ, by using the equation

$$\frac{\text{fwhm}\cos\theta}{\lambda} = \frac{1}{L_c} + \varepsilon\frac{2\sin\theta}{\lambda} \quad (1)$$

where the full width at half-maximum (fwhm) was determined by fitting the peak shape to a Voigt function and λ represents the wavelength. Figure 7 shows the Williamson−Hall plots for core@shell sample **1** at 300 K, 160 and 100 K after irradiation. At 300 K, the strain is minimal in the core and for the (h00) planes of the shell, with values of ε = 0.2% and ε = 0.3% respectively, consistent with a preferential epitaxial growth of the shell along the (h00) faces.[43] A larger ε value of 0.8% is observed from the (hkl) reflections, indicating the presence of anisotropic strain. Upon cooling, the decrease of the core unit cell constant induces significant mismatch and a remarkable increase of the strain in the shell. The 3-fold increase in ε within the core lattice (0.6%) is accompanied by a 4-fold and 5-fold increase in the shell (h00) and (hkl) planes, respectively. The value of the strain parameter reaching 4.2% along the (hkl) directions of the shell confirms the strongly anisotropic nature of the strain. Significantly, the strain state is then released at 100 K when the process is reversed with light. The optical CTIST returns the core to the HS state with its larger lattice constant, thereby decreasing the lattice misfit and releasing the strain in the core and shell, despite some residual strain in the shell. The (hkl) reflections show a strain parameter that remains higher than its 300 K value (1.6%), potentially due to thermal contraction at 100 K.

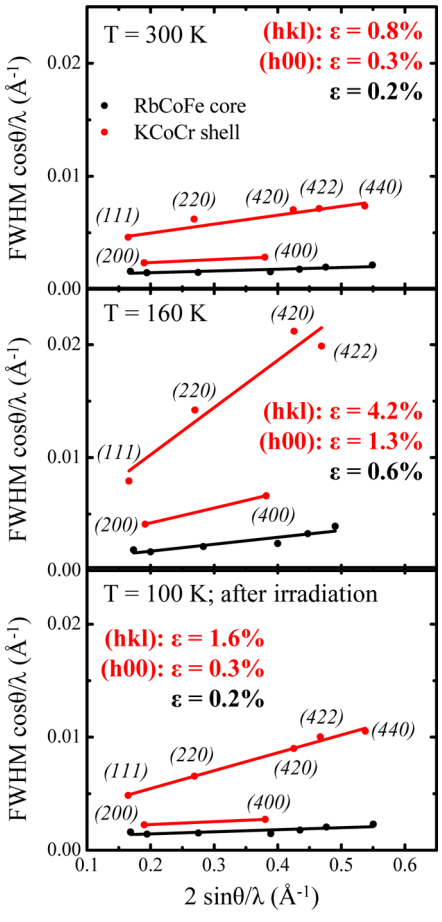

Figure 7. Williamson−Hall plots for core@shell sample **1** at 300 and 160 K in the dark state and at 100 K after irradiation with white light. At 300 K, minimal strain is observed in the core lattice and (h00) planes of the shell. The different slopes for the (h00) and (hkl) lines in the shell lattice are indicative of anisotropic strain. Upon cooling, the contraction of the RbCoFe unit cell associated with the thermal CTIST induces considerable strain on the KCoCr shell, particularly affecting the (hkl) planes. The strain in both the core and shell material is released after irradiation with light at 100 K.

The important observation is that upon cooling to low temperature, the KCoCr shell magnetically orders near 30 K while structurally strained. Therefore, the decrease in magnetization attributed to the shell upon photoirradiation results from a return to the less strained state. The magnetization changes in response to alterations in the local anisotropy of the magnetically ordered lattice. Moments which aligned with the field upon field-cooling through the magnetic ordering temperature then reorient away from the applied field in response to changes in local anisotropy when the lattice strain is released by the optical CTIST.

Returning now to the question of why the thinner shell heterostructures show a light-induced increase instead of a decrease, it must be remembered that the low temperature magnetization is a sum of the contributions of the core and the shell. The RbCoFe core undergoes the characteristic light-induced increase, which for thin shells is a larger influence than the decrease of the shell. Nevertheless, the extent to which changes in the shell contribute to changes in magnetization can be estimated by comparing the core@shell particles with different shell thicknesses (t). A simple 3-component model, Figure 8, was considered with a core of fixed size, a shell of thickness t, and a strained region (SR) in the shell of thickness l, over which the magnetostructural distortions take place. The model uses two main assumptions. First, the photomagnetic properties of the RbCoFe core within the core@shell structure are the same as the uncoated sample, thereby equating the behavior of the core with the magnetic behavior measured for

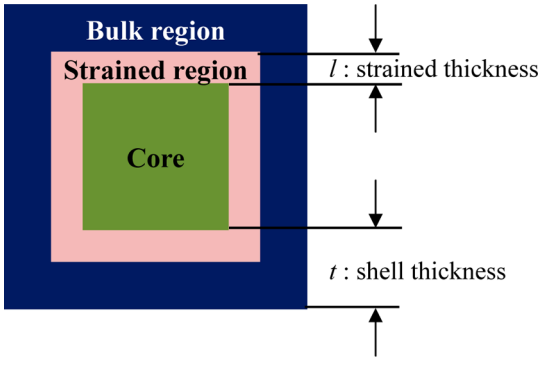

Figure 8. Schematic of the 3-component model for the core@shell heterostructure, dividing the shell into two distinct regions, a bulk-like and strained region (SR). The size of the SR is given by the length l, and t is total thickness of the shell.

dx.doi.org/10.1021/ja5084283 | J. Am. Chem. Soc. 2014, 136, 15660−15669

the uncoated RbCoFe sample. Additionally, the shell comprises two distinct regions: the SR and the bulk region. The model can then be used to quantify the contribution of the SR to the magnetization and to obtain an estimate of its thickness l.

The core contribution to the light−dark magnetization, ΔM_{core}, can be subtracted by using the equation

$$\Delta M_{shell} = \Delta M_{core@shell} - \frac{n_{core}}{n_{core@shell}} \Delta M_{core} \quad (2)$$

where $\Delta M_x = M_x^{light} - M_x^{dark}$, the difference of the magnetic responses in the light and dark states for the x component (core, shell or core@shell) and n_x represents the number of moles calculated from the equation $n_x = mass_x/MW_x$. The ratios between the masses can be calculated from the EDS data, and the molecular weights (MW) are known (see Experimental Section). ΔM_{core} is the light−dark magnetization measured for the uncoated RbCoFe particles. The quantity ΔM_{shell} is plotted in Figure 9 for the temperature-dependent response taken at

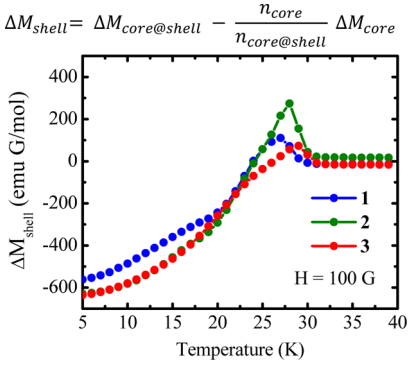

Figure 9. A plot of ΔM_{shell} vs temperature as derived from eq 2 for the three core@shell samples. All the quantities are per mole of the combined core@shell particles.

H = 100 G. According to the model, ΔM_{core} should be independent of the shell thickness if $t > l$, because in this case, the nonphotoactive bulk will be subtracted and only the magnetization of the SR will be left. The fact that the treatment for core@shell samples **2** and **3** lie on top of each other in the 5−25 K interval (Figure 9) suggests that the model works well and that for those two shell thicknesses, $t > l$. On the other hand, the treatment indicates that $t < l$ for the 11 nm shell. For all three samples, however, ΔM_{shell} is negative at low temperatures, consistent with the response observed for the CoFe/NiCr heterostructures studied previously.[24−26,28]

A different treatment affords an estimate of the size of the strained region (SR). Specifically,

$$M_{shell}^{light} = M_{core@shell}^{light} - \frac{n_{core}}{n_{core@shell}} M_{core}^{light} \quad (3)$$

gives the magnetization of the shell in the light state after subtracting the core effects (the dark data have not been subtracted), where the superscripts designate the magnetic responses after irradiation and the subscripts refer to specific contributions of the core, shell, or core@shell ensemble. The value M_{shell}^{light} will be a function of the thickness t. For the shells where $t < l$, the magnetization will be proportional to the size of the shell, while for $t > l$ the magnetization will be the sum of the magnetization of the SR and the bulk region. More explicitly,

$$M_{shell}^{light} = \begin{cases} M_{SR}^{light} \dfrac{n_{shell}}{n_{SR}} & \text{for } t < l \\ M_{SR}^{light} \dfrac{n_{SR}}{n_{shell}} + M_{bulk} \dfrac{n_{bulk}}{n_{shell}} & \text{for } t > l \end{cases} \quad (4)$$

Considering that the molecular weight is the same throughout the shell and the mass is proportional to the volume, we determine the two following equations:

$$M_{shell}^{light} = \begin{cases} M_{SR}^{light} \dfrac{V_{shell}}{V_{SR}} & \text{for } t < l \\ M_{SR}^{light} \dfrac{V_{SR}}{V_{shell}} + M_{bulk} \dfrac{V_{bulk}}{V_{shell}} & \text{for } t > l \end{cases} \quad (5)$$

for which there are two free parameters, M_{SR}^{light} and V_{SR}. Fitting the data for the three core@shell samples at T = 5 K and H = 100 G, using M_{bulk} = 4475 emu G/mol (estimated from magnetic measurements in a single phase KCoCr), gives values of M_{SR}^{light} = 2850 emu G/mol and $V_{SR} = 3.658 \times 10^6$ nm^3. The model predicts a thickness of the strained region of $l \sim 24$ nm (Figure 10) regardless of the exact microscopic mechanism of

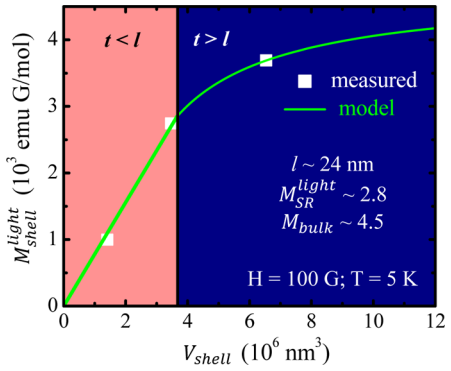

Figure 10. Plot of M_{shell}^{light} from eq 3 vs volume, V_{shell}, for the three core@shell samples and the fitting of the model from eq 5. The pink area corresponds to the SR, and the blue is the bulk region. The treatment estimates the thickness of the SR as $l \sim 24$ nm.

the magnetization change. It is important to remember that the model assumes that the photomagnetic response of the core in all core@shell samples of the series is the same. A refined model will take into account the fact that the shell also induces strain on the core and will modify its magnetic properties.

A prominent feature of the field-cooled magnetization in the light state of each core@shell sample is a slightly higher ordering temperature of the KCoCr. This feature is more clearly seen in the difference plots, Figures 3 and 9, where the higher ordering temperature manifests as an increase in ΔM around 30 K. The higher ordering temperature reflects subtle changes in the local exchange interactions in the shell associated with release of strain in the core upon undergoing the HS to LS CTIST. For the two thinner shell heterostructures, the photoincrease persists at lower temperatures due to the ordering of the RbCoFe core. For the thicker shell sample, **3**, there is a crossover to the photodecrease that is dominated by the local anisotropy changes in the shell.

Influence of the Shell on the Core. Previous reports have demonstrated the influence of various types of matrices over the spin crossover properties of embedded particles.[51−56] Although the heterostructures reported here were designed so

dx.doi.org/10.1021/ja5084283 | J. Am. Chem. Soc. 2014, 136, 15660−15669

that elastic changes of the core actuate property changes in the shell, it is clear that the shell strongly influences the structure and phase transitions of the core. Analysis of the magnetization change associated with the thermal CTIST indicates that the high spin to low spin conversion is complete, yet the associated contraction of the lattice decreases as the shell thickness increases. The room temperature lattice constants of the individual phases are 10.551 Å for $K_{0.10}Co[Cr(CN)_6]_{0.70}\cdot 4H_2O$ and 10.303 Å for high spin $Rb_{0.24}Co[Fe(CN)_6]_{0.74}\cdot 3H_2O$, a difference that is small enough that there is relatively little strain when the two lattices form an interface in the core@shell particles. Upon transitioning to the low-spin state, the RbCoFe lattice contracts to ∼9.95 Å, which then creates a significant difference with the KCoCr unit cell. However, in the core@shell particles, the low-spin RbCoFe lattice parameters range from 9.90 Å for sample **1**, with the thinnest shell, to 10.072 Å for **3**, indicating that the low-spin RbCoFe is significantly strained as part of the core@shell particle. As the shell becomes thicker, it appears to become less elastic, thereby further restricting the ability of the core to contract in response to the spin change.

The presence of the shell not only limits the lattice contraction associated with the thermal CTIST, but it also deeply affects the nature of the transition. The change can be seen in the high temperature χT vs T plot (Figure 2) in which the uncoated RbCoFe particles display the normal hysteresis indicative of bistability. On the other hand, the hysteretic behavior is lost for RbCoFe@KCoCr heterostructures. These observations parallel the evolution of the structural parameters upon cooling (Figure 5). The CTIST in the uncoated RbCoFe particles is a discontinuous, first-order phase transition. In contrast, the RbCoFe@KCoCr heterostructures undergo a continuous phase transition.

In materials displaying spin-crossover, both continuous and discontinuous transitions have been observed resulting from magnetostructural phase changes.[38,57−65] A model described by Boukheddaden et al. sheds light upon the parameters influencing the nature of the thermal CTIST in cobalt hexacyanoferrate.[66,67] The model predicts a continuous or discontinuous evolution of the high spin state fraction depending on the interplay of two key parameters, the ligand-field energy gap and the elastic interaction.[66] Here, we report for the first time a switch between abrupt and smooth transition in cobalt hexacyanoferrate induced by the presence of the shell. The shell is not likely to affect the ligand-field parameter, but a change in the elastic interaction becomes evident with the observation of structural constraints on the core resulting from the presence of the shell. Furthermore, the structural study provides evidence that the synergistic effects between core and shell materials extend well beyond the few unit cells across the interface.

CONCLUSION

The RbCoFe@KCoCr system provides a new example of a coordination polymer heterostructure in which synergistic effects between the core and shell lead to new behavior, in this case light-induced alteration of the magnetization of the normally light-insensitive KCoCr. The KCoCr magnetization change is shown to be a magnetomechanical effect as the CTIST of the RbCoFe core induces structural strains in the shell accompanying the magnetization change. The design and fine control of a series of core@shell particles with varying shell thickness allows an estimate of the depth of the shell material that responds to the core changes. Analysis of the magnetic response in light and dark states indicates this depth to be approximately 24 nm. At the same time, the presence of the shell alters the behavior of the core, changing the nature of the CTIST. A shell as thin as 11 nm alters the phase transition of a 135 nm particle. Overall, this study provides a better understanding of the length scales involved in the synergistic effects between core and shell and further evidence that these effects are not limited to the few unit cells across the core@shell interface.

ASSOCIATED CONTENT

Supporting Information

(**1**) EDS line scans on RbCoFe@KCoCr core@shell particles; (**2**) TEM image of RbCoFe cores; (**3**) Size dispersion for RbCoFe cores and RbCoFe@KCoCr heterostructures; (**4**) Predicted particle size for the RbCoFe@KCoCr structures; (**5**) FT-IR spectra for for RbCoFe cores and RbCoFe@KCoCr heterostructures; (**6**) PXRD patterns at 300 K for RbCoFe cores and RbCoFe@KCoCr heterostructures; (**7**) PXRD patterns at 160 K for RbCoFe cores and RbCoFe@KCoCr heterostructures; (**8**) Refined lattice constants at 300 and 160 K for RbCoFe cores and RbCoFe@KCoCr heterostructures; (**9**) PXRD patterns stacked as a function of temperature, from 300 to 160 K, for the core@shell samples **1** and **3**; (**10**) Simulation of χT vs T values in the CTIST region (300−150 K) and detailed analysis; and (**11**) Magnetization vs Field at T = 5 K for **1**, **2**, and **3** in the dark and light state, after irradiation at 5 K. This material is available free of charge via the Internet at http://pubs.acs.org/.

AUTHOR INFORMATION

Corresponding Authors

meisel@phys.ufl.edu
talham@chem.ufl.edu

Notes

The authors declare no competing financial interest.

ACKNOWLEDGMENTS

This work was supported by the National Science Foundation via DMR-1005581 and DMR-1405439 (D.R.T.), DMR-1202033 (M.W.M.) and DMR-1157490 (NHMFL), and by the UF Division of Sponsored Research. This research used resources of the Advanced Photon Source, a U.S. Department of Energy (DOE) Office of Science User Facility operated for the DOE Office of Science by Argonne National Laboratory under Contract No. DE-AC02-06CH11357. The authors thank Ashley Felts, Akhil Ahir, Dr. Isabelle Maurin, Dr. Gregory Halder and the 17-BM staff for assisting with the PXRD collection and analysis. M.W.M. and P.A.Q. acknowledge enlightening conversations with Y. Lee, D. M. Pajerowski and M. K. Peprah.

REFERENCES

(1) Batten, S. R.; Murray, K. S. *Coord. Chem. Rev.* **2003**, *246*, 103.
(2) Kitagawa, S.; Kitaura, R.; Noro, S.-i. *Angew. Chem., Int. Ed.* **2004**, *43*, 2334.
(3) Maspoch, D.; Ruiz-Molina, D.; Veciana, J. *J. Mater. Chem.* **2004**, *14*, 2713.
(4) Cheetham, A. K.; Rao, C. N. R.; Feller, R. K. *Chem. Commun.* **2006**, 4780.
(5) Robin, A. Y.; Fromm, K. M. *Coord. Chem. Rev.* **2006**, *250*, 2127.

(6) Dubbeldam, D.; Walton, K. S.; Ellis, D. E.; Snurr, R. Q. *Angew. Chem., Int. Ed.* **2007**, *46*, 4496.
(7) Corma, A.; Garcia, H.; Llabres, i.; Xamena, F. X. *Chem. Rev.* **2010**, *110*, 4606.
(8) Janiak, C.; Vieth, J. K. *New J. Chem.* **2010**, *34*, 2366.
(9) Tokoro, H.; Ohkoshi, S.-i. *Dalton Trans.* **2011**, *40*, 6825.
(10) Ohkoshi, S.-i.; Tokoro, H. *Acc. Chem. Res.* **2012**, *45*, 1749.
(11) Wang, C.; Liu, D.; Lin, W. *J. Am. Chem. Soc.* **2013**, *135*, 13222.
(12) Horike, S.; Umeyama, D.; Kitagawa, S. *Acc. Chem. Res.* **2013**, *46*, 2376.
(13) Grancha, T.; Ferrando-Soria, J.; Castellano, M.; Julve, M.; Pasan, J.; Armentano, D.; Pardo, E. *Chem. Commun.* **2014**, *50*, 7569.
(14) Horcajada, P.; Gref, R.; Baati, T.; Allan, P. K.; Maurin, G.; Couvreur, P.; Ferey, G.; Morris, R. E.; Serre, C. *Chem. Rev.* **2012**, *112*, 1232.
(15) Novio, F.; Simmchen, J.; Vazquez-Mera, N.; Amorin-Ferre, L.; Ruiz-Molina, D. *Coord. Chem. Rev.* **2013**, *257*, 2839.
(16) Jung, J. H.; Lee, J. H.; Silverman, J. R.; John, G. *Chem. Soc. Rev.* **2013**, *42*, 924.
(17) Dumont, M. F.; Hoffman, H. A.; Yoon, P. R. S.; Conklin, L. S.; Saha, S. R.; Paglione, J.; Sze, R. W.; Fernandes, R. *Bioconjugate Chem.* **2014**, *25*, 129.
(18) Hoffman, H. A.; Chakrabarti, L.; Dumont, M. F.; Sandler, A. D.; Fernandes, R. *RSC Adv.* **2014**, *4*, 29729.
(19) Imanishi, N.; Morikawa, T.; Kondo, J.; Yamane, R.; Takeda, Y.; Yamamoto, O.; Sakaebe, H.; Tabuchi, M. *J. Power Sources* **1999**, *81*−*82*, 530.
(20) Okubo, M.; Asakura, D.; Mizuno, Y.; Kudo, T.; Zhou, H.; Okazawa, A.; Kojima, N.; Ikedo, K.; Mizokawa, T.; Honma, I. *Angew. Chem., Int. Ed.* **2011**, *50*, 6269.
(21) Asakura, D.; Li, C. H.; Mizuno, Y.; Okubo, M.; Zhou, H.; Talham, D. R. *J. Am. Chem. Soc.* **2013**, *135*, 2793.
(22) Okubo, M.; Li, C. H.; Talham, D. R. *Chem. Commun.* **2014**, *50*, 1353.
(23) Jiles, D. C. *J. Phys. D: Appl. Phys.* **1995**, *28*, 1537.
(24) Pajerowski, D. M.; Andrus, M. J.; Gardner, J. E.; Knowles, E. S.; Meisel, M. W.; Talham, D. R. *J. Am. Chem. Soc.* **2010**, *132*, 4058.
(25) Dumont, M. F.; Knowles, E. S.; Guiet, A.; Pajerowski, D. M.; Gomez, A.; Kycia, S. W.; Meisel, M. W.; Talham, D. R. *Inorg. Chem.* **2011**, *50*, 4295.
(26) Pajerowski, D. M.; Gardner, J. E.; Frye, F. A.; Andrus, M. J.; Dumont, M. F.; Knowles, E. S.; Meisel, M. W.; Talham, D. R. *Chem. Mater.* **2011**, *23*, 3045.
(27) Dia, N.; Lisnard, L.; Prado, Y.; Gloter, A.; Stephan, O.; Brisset, F.; Hafez, H.; Saad, Z.; Mathoniere, C.; Catala, L.; Mallah, T. *Inorg. Chem.* **2013**, *52*, 10264.
(28) Knowles, E. S.; Li, C. H.; Dumont, M. F.; Peprah, M. K.; Andrus, M. J.; Talham, D. R.; Meisel, M. W. *Polyhedron* **2013**, *66*, 153.
(29) Gros, C. R.; Peprah, M. K.; Hosterman, B. D.; Brinzari, T. V.; Quintero, P. A.; Sendova, M.; Meisel, M. W.; Talham, D. R. *J. Am. Chem. Soc.* **2014**, *136*, 9846.
(30) Ohkoshi, S. i.; Hashimoto, K. *Chem. Phys. Lett.* **1999**, *314*, 210.
(31) Sato, O.; Iyoda, T.; Fujishima, A.; Hashimoto, K. *Science* **1996**, *272*, 704.
(32) Yoshizawa, K.; Mohri, F.; Nuspl, G.; Yamabe, T. *J. Phys. Chem. B* **1998**, *102*, 5432.
(33) Kawamoto, T.; Asai, Y.; Abe, S. *Phys. Rev. B: Condens. Matter Mater. Phys.* **1999**, *60*, 12990.
(34) Bleuzen, A.; Lomenech, C.; Escax, V.; Villain, F.; Varret, F.; Cartier dit Moulin, C.; Verdaguer, M. *J. Am. Chem. Soc.* **2000**, *122*, 6648.
(35) Cartier dit Moulin, C.; Villain, F.; Bleuzen, A.; Arrio, M.-A.; Sainctavit, P.; Lomenech, C.; Escax, V.; Baudelet, F.; Dartyge, E.; Gallet, J.-J.; Verdaguer, M. *J. Am. Chem. Soc.* **2000**, *122*, 6653.
(36) Champion, G.; Escax, V.; Cartier dit Moulin, C.; Bleuzen, A.; Villain, F.; Baudelet, F.; Dartyge, E.; Verdaguer, M. *J. Am. Chem. Soc.* **2001**, *123*, 12544.
(37) Shimamoto, N.; Ohkoshi, S.; Sato, O.; Hashimoto, K. *Inorg. Chem.* **2002**, *41*, 678.
(38) Escax, V.; Bleuzen, A.; Itie, J. P.; Munsch, P.; Varret, F.; Verdaguer, M. *J. Phys. Chem. B* **2003**, *107*, 4763.
(39) Escax, V.; Champion, G.; Arrio, M.-A.; Zacchigna, M.; Cartier dit Moulin, C.; Bleuzen, A. *Angew. Chem., Int. Ed.* **2005**, *44*, 4798.
(40) Maurin, I.; Chernyshov, D.; Varret, F.; Bleuzen, A.; Tokoro, H.; Hashimoto, K.; Ohkoshi, S.-i. *Phys. Rev. B: Condens. Matter Mater. Phys.* **2009**, *79*, 064420/1.
(41) Cafun, J.-D.; Champion, G.; Arrio, M.-A.; Cartier dit Moulin, C.; Bleuzen, A. *J. Am. Chem. Soc.* **2010**, *132*, 11552.
(42) Catala, L.; Brinzei, D.; Prado, Y.; Gloter, A.; Stephan, O.; Rogez, G.; Mallah, T. *Angew. Chem., Int. Ed.* **2009**, *48*, 183.
(43) Presle, M.; Maurin, I.; Maroun, F.; Cortes, R.; Lu, L.; Sayed Hassan, R.; Larquet, E.; Guigner, J.-M.; Riviere, E.; Wright, J. P.; Boilot, J.-P.; Gacoin, T. *J. Phys. Chem. C* **2014**, *118*, 13186.
(44) Knowles, E. S. Ph.D. Dissertation, University of Florida, Gainesville, FL, 2013.
(45) Brinzei, D.; Catala, L.; Louvain, N.; Rogez, G.; Stephan, O.; Gloter, A.; Mallah, T. *J. Mater. Chem.* **2006**, *16*, 2593.
(46) Risset, O. N.; Knowles, E. S.; Ma, S.; Meisel, M. W.; Talham, D. R. *Chem. Mater.* **2013**, *25*, 42.
(47) Pajerowski, D. M.; Ravel, B.; Li, C. H.; Dumont, M. F.; Talham, D. R. *Chem. Mater.* **2014**, *26*, 2586.
(48) Sato, Y.; Ohkoshi, S.; Arai, K.; Tozawa, M.; Hashimoto, K. *J. Am. Chem. Soc.* **2003**, *125*, 14590.
(49) Prado, Y.; Arrio, M.-A.; Volatron, F.; Otero, E.; Cartier, d. M. C.; Sainctavit, P.; Catala, L.; Mallah, T. *Chem.—Eur. J.* **2013**, *19*, 6685.
(50) Williamson, G. K.; Hall, W. H. *Acta Metall.* **1953**, *1*, 22.
(51) Suzuki, A.; Fujiwara, M.; Nishijima, M. *Colloid Polym. Sci.* **2008**, *286*, 525.
(52) Raza, Y.; Volatron, F.; Moldovan, S.; Ersen, O.; Huc, V.; Martini, C.; Brisset, F.; Gloter, A.; Stephan, O.; Bousseksou, A.; Catala, L.; Mallah, T. *Chem. Commun.* **2011**, *47*, 11501.
(53) Felix, G.; Nicolazzi, W.; Salmon, L.; Molnar, G.; Perrier, M.; Maurin, G.; Larionova, J.; Long, J.; Guari, Y.; Bousseksou, A. *Phys. Rev. Lett.* **2013**, *110*, 235701/1.
(54) Oubouchou, H.; Slimani, A.; Boukheddaden, K. *Phys. Rev. B: Condens. Matter Mater. Phys.* **2013**, *87*, 104104/1.
(55) Felix, G.; Mikolasek, M.; Molnar, G.; Nicolazzi, W.; Bousseksou, A. *Chem. Phys. Lett.* **2014**, *607*, 10.
(56) Slimani, A.; Boukheddaden, K.; Yamashita, K. *Phys. Rev. B: Condens. Matter Mater. Phys.* **2014**, *89*, 214109.
(57) Gutlich, P.; Garcia, Y.; Goodwin, H. A. *Chem. Soc. Rev.* **2000**, *29*, 419.
(58) Ohkoshi, S.; Tokoro, H.; Utsunomiya, M.; Mizuno, M.; Abe, M.; Hashimoto, K. *J. Phys. Chem. B* **2002**, *106*, 2423.
(59) Chernyshov, D.; Hostettler, M.; Tornroos, K. W.; Burgi, H.-B. *Angew. Chem., Int. Ed.* **2003**, *42*, 3825.
(60) Real, J. A.; Gaspar, A. B.; Niel, V.; Munoz, M. C. *Coord. Chem. Rev.* **2003**, *236*, 121.
(61) Margadonna, S.; Prassides, K.; Fitch, A. N. *Angew. Chem., Int. Ed.* **2004**, *43*, 6316.
(62) Kosaka, W.; Nomura, K.; Hashimoto, K.; Ohkoshi, S. *J. Am. Chem. Soc.* **2005**, *127*, 8590.
(63) Papanikolaou, D.; Margadonna, S.; Kosaka, W.; Ohkoshi, S.-I.; Brunelli, M.; Prassides, K. *J. Am. Chem. Soc.* **2006**, *128*, 8358.
(64) Bousseksou, A.; Molnar, G.; Salmon, L.; Nicolazzi, W. *Chem. Soc. Rev.* **2011**, *40*, 3313.
(65) Halcrow, M. A. *Chem. Soc. Rev.* **2011**, *40*, 4119.
(66) Boukheddaden, K.; Nishino, M.; Miyashita, S.; Varret, F. *Phys. Rev. B: Condens. Matter Mater. Phys.* **2005**, *72*, 014467/1.
(67) Nishino, M.; Boukheddaden, K.; Miyashita, S.; Varret, F. *Phys. Rev. B: Condens. Matter Mater. Phys.* **2005**, *72*, 064452/1.